Filament Based Plasma

MARCEL PADILLA*, TU Berlin
OLIVER GROSS*, TU Berlin
FELIX KNÖPPEL, TU Berlin
ALBERT CHERN, UC San Diego
ULRICH PINKALL, TU Berlin
PETER SCHRÖDER, Caltech

Simulation of stellar atmospheres, such as that of our own sun, is a common task in CGI for scientific visualization, movies and games. A fibrous volumetric texture is a visually dominant feature of the solar corona—the plasma that extends from the solar surface into space. These coronal fibers can be modeled as magnetic filaments whose shape is governed by the magnetohydrostatic equation. The magnetic filaments provide a Lagrangian curve representation and their initial configuration can be prescribed by an artist or generated from magnetic flux given as a scalar texture on the sun's surface. Subsequently, the shape of the filaments is determined based on a variational formulation. The output is a visual rendering of the whole sun. We demonstrate the fidelity of our method by comparing the resulting renderings with actual images of our sun's corona.

CCS Concepts: • **Applied computing** → **Astronomy**; **Physics**; • **Mathematics of computing** → **Partial differential equations**; • **Computing methodologies** → **Scientific visualization**.

Additional Key Words and Phrases: Magnetohydrostatics, Conformal, Geodesics, Lagrangian modeling, Filament based method.

1 INTRODUCTION

The desire to visualize astrophysical objects and phenomena is intricately linked with the early history of computer graphics [Gómez et al. 2017] and continues today with landmark visualizations of the solar atmosphere [NASA Scientific Visualization Studio 2018; CADENS 2015; Borkiewicz et al. 2019]. In particular, the arcs visible in our sun's atmosphere are some of the most awe-inspiring natural spectacles, making their visual depiction of great interest in scientific visualization, special effects, and games.

For a physically motivated algorithm, consider that stars like our sun are surrounded by a *corona*. This is an atmosphere consisting

*Both authors contributed equally to this research.

Authors' addresses: Marcel Padilla, TU Berlin, Berlin, Germany, padilla@math.tu-berlin.de; Oliver Gross, TU Berlin, Berlin, Germany, ogross@math.tu-berlin.de; Felix Knöppel, TU Berlin, Berlin, Germany, knoeppel@math.tu-berlin.de; Albert Chern, UC San Diego, San Diego, CA, USA, alchern@ucsd.edu; Ulrich Pinkall, TU Berlin, Berlin, Germany, pinkall@math.tu-berlin.de; Peter Schröder, Caltech, Pasadena, CA, USA, ps@caltech.edu.
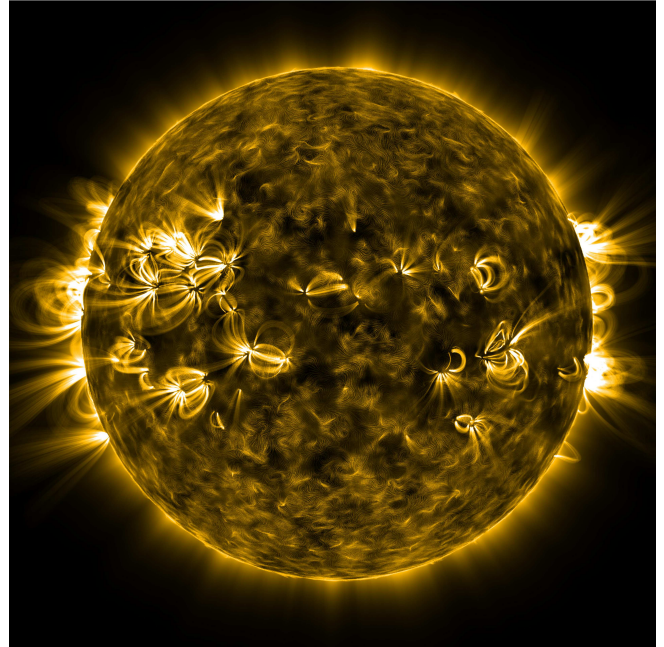
Fig. 1. A procedurally generated solar atmosphere computed by our algorithm. The underlying magnetic flux map was randomly generated and is shown in the inset on this page.

of *plasma*, an ionized and electrically conducting gas that interacts with a variable magnetic field through the *magnetohydrodynamic* (MHD) equations. Due to the large time scales involved, the visually prominent phenomena are governed by the *magnetohydrostatic* (MHS) equation [Rosner et al. 1978]

$$\mathbf{0} = \tfrac{1}{\mu_0}(\operatorname{curl}\mathbf{B}) \times \mathbf{B} - \operatorname{grad} p + \tfrac{m}{k_{\mathrm{B}}T}p\mathbf{g}. \tag{1}$$

Here $\mathbf{B}$ is the magnetic field, p the gas pressure, T the temperature, μ_0 the vacuum permeability, k_{B} the Boltzmann constant, m the mass of a proton and $\mathbf{g}$ the gravitational acceleration field.

This equation has many possible solutions, even for given flux boundary conditions. To overcome this indeterminacy we select a special class of solutions. Numerically, these solutions can be described by a set of curves which minimize a variational energy. In principle, these curves can
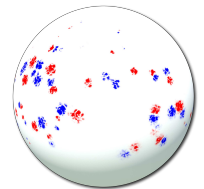
be initialized arbitrarily, which means that geometric modeling tools can be used for the design of stellar atmospheres.

If the magnetic flux is already given as a scalar texture on the sun's surface (inset first page) initial curves can be chosen as geodesics with respect to a particular conformal metric, while their start and end points can be found through a linear assignment problem.

To summarize, we assemble a computational pipeline for procedurally generating the visual appearance of our sun. Using Lagrangian elements, the features of the solar atmosphere are reconstructed at a high level of detail. An accompanying video and a complete implementation of this research is available at https://page.math.tu-berlin.de/~padilla/.

2 RELATED WORK

The visible fibers in the solar atmosphere follow field lines of the magnetic field, mainly known through its flux on the solar surface. Therefore, a problem extensively discussed in the solar physics literature (see e.g. [Warren et al. 2018; Yeates et al. 2018]) is the following:

> *Given a flux density on the surface of the sun, extend it to a magnetic field* **B** *in the solar atmosphere that, for suitable choice of gas pressure p and temperature distribution T, satisfies the MHS equation.*

Unfortunately, this problem is underdetermined and one has to focus on special classes of solutions.

In special cases analytic solutions are known [Kippenhahn and Schlüter 1957; Low 1982], for an overview see e.g. [Priest 2014, Sec. 3.5]. In general, numerical approaches are needed.

2.1 Force-Free Fields

A special class of solutions is obtained if one assumes that gas pressure is negligible. In this case the MHS equation (1) reduces to

$$(\text{curl } \mathbf{B}) \times \mathbf{B} = 0. \tag{2}$$

Divergence-free vector fields **B** satisfying (2) are called *force-free*.

2.1.1 Potential Fields. The easiest approach to force-free fields is through the solution of a Neumann problem. Here one solves for a harmonic vector field, that is, a divergence-free field **B** with

$$\text{curl } \mathbf{B} = \mathbf{0},$$

on the exterior of the sun with appropriate boundary conditions. Looking for a field on the whole sun exterior with prescribed flux through the sun's surface [Nabizadeh et al. 2021, Figs. 12, 13] gives unrealistic results far away from the sun (compare Fig. 20, middle). Better results are obtained if additional boundary conditions are prescribed on an outer boundary at about 2.5 sun radii (compare Fig. 20, left). This approach is known as the *Potential Field Source Surface* model (PFSS) [Altschuler and Newkirk 1969; Sakurai 1982] (see also [Priest 2014, Sec. 3.3]). PFSS fields are published on a daily basis [NASA Solar Dynamics Observatory 2022].

2.1.2 Nonlinear Force-Free Fields. General solutions of Eq. (2) are called *Nonlinear Force-Free Fields* (NLFFF). In order to specify such a solution, in addition to the boundary flux, a field topology has to be prescribed. This allows for the handling of twisted or braided fields (cf. Sec. 4.2.2). While numerical treatments commonly use

Eulerian methods [Titov et al. 2018; Grad and Rubin 1958; Inhester and Wiegelmann 2006], DeForest and Kankelborg [2007] propose a Lagrangian method which discretizes the volumetric field into a set of curves called *fluxons*. Other methods such as the *Aschwanden Vertical-current Forward Fit* (VCA) [2016] method employ additional image data as constraints. For comparisons of NLFFF with other methods see [Yeates et al. 2018; Warren et al. 2018]. To facilitate further comparison we used some of the same data in our method (Figs. 14, 17, 19, 20 and 21).

In order to compensate for missing gas pressure, NLFFF methods have to use artificial confining fields as in [Rachmeler et al. 2009].
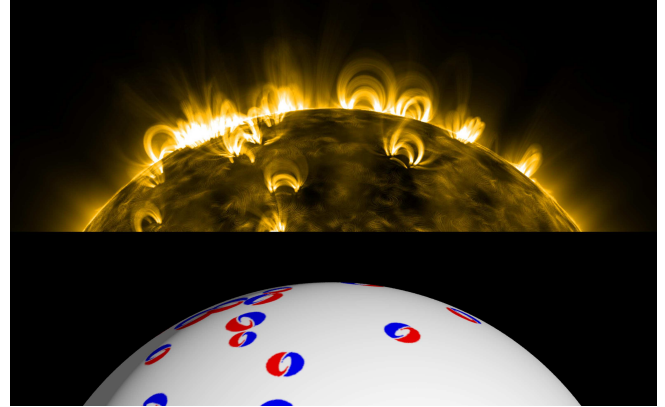

Fig. 2. An artistically designed flux map (bottom) and the corresponding solar atmosphere (top). An animated version is provided in the supplementary material.

2.2 Incorporating Hydraulic Effects

Numerical solutions of the full MHS equation (1), incorporating hydraulic effects of the plasma and gravity, typically employ Eulerian MHD relaxation methods [Chodura and Schlüter 1981; Parker 1994; Janse et al. 2010]. One class of models which incorporates hydraulic effects consists of the so-called *Current-Sheet* (CS) models (see e.g. [Moradi et al. 2010]). In these, the magnetic field is confined in a domain bounded by a surface—the *current sheet*. Outside of this domain, in the gas domain, the magnetic field vanishes.

Our own method combines the force-free model with a current-sheet model by assuming that inside of the magnetic domain the field is force-free. In this way, the effect of gas pressure is encoded in the geometry of the magnetic domain. This allows us to describe the field in terms of a Lagrangian description by a collection of curves.

Like the NLFFF methods, we are able to handle twisted or braided field topologies and quasi-static dynamics (cf. Fig. 13), which both are valuable features for CGI.

2.3 Lagrangian Curves for Fibered Volumes

At its core our approach is characterized by using Lagrangian curves to model a fibered volume. While applied to solar atmospheres here, such an approach is not new to computer graphics. It is also applied, for example, in hair modeling [Hadap and Magnenat-Thalmann 2001], muscle modeling [Angles et al. 2019; Yu et al. 2021], or for

vorticity in fluids [Angelidis and Neyret 2005; Weißmann and Pinkall 2010; Padilla et al. 2019].

2.4 Glow Model and Rendering

For the purpose of rendering the solar atmosphere one needs to know how the computed magnetic field is related to emission (glow). Methods for the volumetric rendering of the solar atmosphere have been discussed in [Schrijver et al. 2005; Lionello et al. 2008; Machado et al. 2012; Peter et al. 2012; Naiman et al. 2017]. The physics of plasma glow is investigated in [Boerner et al. 2012; Zhuleku et al. 2020].

3 FORCE-FREE CURRENT-SHEET MODEL

As explained in Sec. 2.2 we consider a special CS model, referred to as the *Force-Free Current-Sheet* (FFCS) model, where the magnetic field is assumed to be force-free. In this model the solar corona (*plasma domain*) is decomposed into a *gas domain*, in which there is only gas but no magnetic field, and a *flux domain*, in which there is magnetic field but no gas.

3.1 Plasma Domain

Let $\mathbb{M}$ be the *plasma domain* and $\mathbb{M}_0, \mathbb{M}_\mathbf{B} \subset \mathbb{M}$ be domains whose interiors are disjoint while $\mathbb{M} = \mathbb{M}_0 \cup \mathbb{M}_\mathbf{B}$. The plasma domain is thus partitioned into the *gas domain* $\mathbb{M}_0$ and the *flux domain* $\mathbb{M}_\mathbf{B}$. The state of the plasma is given by the domain decomposition together with the magnetic field $\mathbf{B}$.

3.2 Gas Domain

In the gas domain $\mathbb{M}_0$ we have $|\mathbf{B}| = 0$ and the only relevant quantity is the gas pressure $p_{\text{gas}} \colon \mathbb{M}_0 \to \mathbb{R}_{>0}$, which satisfies (1). Under mild topological assumptions p_{gas} can be extended to a function $p \colon \mathbb{M} \to \mathbb{R}_{>0}$ depending on the height above the surface only (cf. App. A).

3.3 Flux Domain

The flux domain is a manifold with corners—we allow for creases on $\Sigma_\mathbf{B} \coloneqq \partial \mathbb{M}_\mathbf{B} \cap \partial \mathbb{M}$. Away from the creases the boundary $\partial \mathbb{M}_\mathbf{B}$ is smooth. The flux domain is void of gas and the support of a divergence-free vector field $\mathbf{B} \colon \mathbb{M}_\mathbf{B} \to \mathbb{R}^3$. This field realizes the prescribed boundary flux on $\Sigma_\mathbf{B}$ and is tangent to the boundary $\partial \mathbb{M}_\mathbf{B}$ elsewhere.

3.4 FFCS-Solutions of the MHS Equation

In App. B we prove

THEOREM 1. *A state of the plasma* $(\mathbb{M}_\mathbf{B}, \mathbf{B})$ *solves the MHS equation* (1) *(in a distributional sense) if and only if* $\mathbf{B}$ *is force-free and satisfies* $|\mathbf{B}|^2/2\mu_0 = p_{gas}$ *on* $\partial \mathbb{M}_0 \cap \partial \mathbb{M}_\mathbf{B}$.

4 VARIATIONAL FORMULATION

We now turn to a variational formulation of the FFCS model.

4.1 Magnetohydrostatic Energy

Let $p \colon \mathbb{M} \to \mathbb{R}_{>0}$ denote the extension of the gas pressure on $\mathbb{M}_0$ to a function on the whole of $\mathbb{M}$ (cf. App. A). For a domain decomposition

$\mathbb{M} = \mathbb{M}_0 \cup \mathbb{M}_\mathbf{B}$ with corresponding magnetic field $\mathbf{B}$ we define the energy:

$$\mathcal{E}(\mathbb{M}_\mathbf{B}, \mathbf{B}) \coloneqq \int_{\mathbb{M}_\mathbf{B}} \left(p + \frac{|\mathbf{B}|^2}{2\mu_0} \right). \tag{3}$$

To see the physical meaning of this energy, imagine $\mathbb{M}$ initially without any $\mathbf{B}$ and filled throughout with gas at pressure p. Growing a vacuum-filled hole—initially of zero volume—with shape $\mathbb{M}_\mathbf{B}$ involves doing work against the pressure p. The total energy needed for creating the hole will be $\int_{\mathbb{M}_\mathbf{B}} p$. Filling $\mathbb{M}_\mathbf{B}$ with the magnetic field $\mathbf{B}$ adds further magnetic energy, the amount being $\int_{\mathbb{M}_\mathbf{B}} |\mathbf{B}|^2/2\mu_0$.

4.2 Variational Principle

As explained in App. C, it is natural to consider variations of $\mathbf{B}$ of the form

$$\mathring{\mathbf{B}} = \text{curl}(Y \times \mathbf{B}),$$

induced by a vector field Y on $\mathbb{M}$.

THEOREM 2. *Let* $\mathbb{M} = \mathbb{M}_0 \cup \mathbb{M}_\mathbf{B}$ *be a domain decomposition with magnetic field* $\mathbf{B}$ *and* N *be the outward-pointing normal of* $\mathbb{M}_\mathbf{B}$. *Then the energy variation corresponding to a vector field* Y *on* $\mathbb{M}$ *is given by*

$$\mathring{\mathcal{E}} = - \int_{\mathbb{M}_\mathbf{B}} \langle \tfrac{1}{\mu_0} \text{curl}\,\mathbf{B} \times \mathbf{B}, Y \rangle$$
$$+ \int_{\partial \mathbb{M}_\mathbf{B}} \left(\left(p - \frac{|\mathbf{B}|^2}{\mu_0} \right) \langle Y, N \rangle + \tfrac{1}{\mu_0} \langle \mathbf{B}, Y \rangle \langle \mathbf{B}, N \rangle \right).$$

PROOF. See App. D. □

4.2.1 Fixed Boundary. Let us consider the case where only variations are allowed that leave the interior of the sun unchanged. This amounts to variations which fix the boundary $\partial \mathbb{M}$ pointwise. In that case a straightforward implication of Thm. 2 is:

THEOREM 3. *A domain decomposition* $\mathbb{M} = \mathbb{M}_0 \cup \mathbb{M}_\mathbf{B}$ *together with a magnetic field* $\mathbf{B}$ *on* $\mathbb{M}_\mathbf{B}$ *is a critical point of* (3) *under variations which fix the boundary* $\partial \mathbb{M}$ *pointwise if and only if it is force-free and satisfies*

$$p = |\mathbf{B}|^2/2\mu_0 \tag{4}$$

on $\partial \mathbb{M}_0 \cap \partial \mathbb{M}_\mathbf{B}$.

In view of Thm. 1 this means that critical points satisfy the MHS equation (1). In the case $\mathbb{M} = \mathbb{M}_\mathbf{B}$, i.e. there is no gas, Thm. 3 amounts to the *Minimum Energy Theorem for Force-Free Fields* (see e.g. [Priest 2014, Sec. 2.8]). Our setup is more general because it accounts for a varying shape of the flux domain.

4.2.2 Fixed Boundary Flux. Allowing only variations that fix the boundary $\partial \mathbb{M}$ pointwise is quite restrictive. It means that we not only prescribe which points on the sun's surface $\partial \mathbb{M}$ are connected by magnetic field lines but also the way field lines are braided and twisted [Prior and Yeates 2016a,b]. This is often expressed by saying that the *topology* of $\mathbf{B}$ is prescribed.

A less restrictive class of variations consists of those diffeomorphisms $\mathbb{M} \to \mathbb{M}$ whose restrictions to $\partial \mathbb{M}$ preserve

the intersections $\Sigma_{\mathbf{B}}$ of the flux domain with $\partial \mathbb{M}$ and in addition preserve the *flux density*

$$\Phi(\mathbf{x}) := \begin{cases} \langle \mathbf{B}(\mathbf{x}), N \rangle & \text{if } \mathbf{x} \in \Sigma_{\mathbf{B}} \\ 0 & \text{if } \mathbf{x} \in \partial \mathbb{M} \setminus \partial \mathbb{M}_{\mathbf{B}}. \end{cases}$$

Using these more general variations the twisting and braiding of field lines can be undone to a large extent, making it possible to lower the energy further. Under mild assumptions, the resulting energy minimizers have a potential field inside of $\mathbb{M}_{\mathbf{B}}$. In the case $\mathbb{M} = \mathbb{M}_{\mathbf{B}}$, i.e. there is no gas, this follows from the *Minimum Energy Theorem for Potential Fields* (see e.g. [Priest 2014, Sec. 2.8]).

To summarize: PFSS is contained in NLFFF as the special case of untwisted field lines. The FFCS model generalizes NLFFF to a situation where the magnetic field is confined by gas in a domain of variable shape.

4.3 Energy in Terms of Field Lines

In Sec. 6 we will discretize our plasma configuration $(\mathbb{M}_{\mathbf{B}}, \mathbf{B})$ as a finite collection of field lines of the magnetic field $\mathbf{B}$ inside of $\mathbb{M}_{\mathbf{B}}$. In preparation, we reformulate here the magnetohydrostatic energy (3) as an integral over the set of field lines Γ.

Assuming that $\mathbf{B}$ is nowhere zero on $\mathbb{M}_{\mathbf{B}}$, we can use the arclength measure ds along the field lines to factor the volume element dV of $\mathbb{R}^3$ as

$$dV = ds \cdot dA,$$
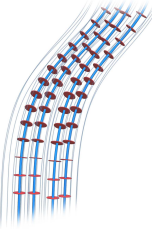
where dA measures area orthogonal to the field lines. Then

$$d\gamma = |\mathbf{B}| dA$$

is the *flux measure* on the set Γ of all field lines and we obtain

$$\mathcal{E}(\mathbb{M}_{\mathbf{B}}, \mathbf{B}) = \int_{\mathbb{M}_{\mathbf{B}}} \left(\frac{p}{|\mathbf{B}|} + \frac{|\mathbf{B}|}{2\mu_0} \right) ds \, d\gamma.$$

For an individual field line $\gamma : [a, b] \to \mathbb{M}_{\mathbf{B}}$ we interpret

$$\mathcal{L}(\gamma) := \int_a^b \left(\frac{p}{|\mathbf{B}|} + \frac{|\mathbf{B}|}{2\mu_0} \right) \circ \gamma \, ds$$

as the length of γ with respect to a Riemannian metric

$$d\tilde{s} := e^u \, ds := \begin{cases} \sqrt{\frac{2p}{\mu_0}} \, ds & \text{in } \mathbb{M}_0 \\ \left(\frac{p}{|\mathbf{B}|} + \frac{|\mathbf{B}|}{2\mu_0} \right) ds & \text{in } \mathbb{M}_{\mathbf{B}}, \end{cases} \quad (5)$$

which is defined on the whole of $\mathbb{M}$ by multiplying the Euclidean metric ds by a *conformal factor* e^u. Note that the conformal factor is a continuous function if the magnetohydrostatic equilibrium (4) holds. With this notation we can write

$$\mathcal{E}(\mathbb{M}_{\mathbf{B}}, \mathbf{B}) = \int_\Gamma \mathcal{L}(\gamma) \, d\gamma, \quad (6)$$

where the integral denotes integration over the set Γ of all field lines.

4.3.1 Pressure-Excess Factor. In (5), the conformal factor in $\mathbb{M}_{\mathbf{B}}$ is the magnetic pressure exceeding the gas pressure. This is apparent from

$$\left(\frac{p}{|\mathbf{B}|} + \frac{|\mathbf{B}|}{2\mu_0} \right) = \sqrt{\frac{2p}{\mu_0}} \left(1 + \frac{(|\mathbf{B}| - \sqrt{2\mu_0 p})^2}{2|\mathbf{B}|\sqrt{2\mu_0 p}} \right). \quad (7)$$

In particular, as the latter summand of the second factor is non-negative, the conformal factor in $\mathbb{M}_{\mathbf{B}}$ is bounded from below by the conformal factor in $\mathbb{M}_0$.

corona
photosphere
sunspot
buoyancy
magnetic flux tube
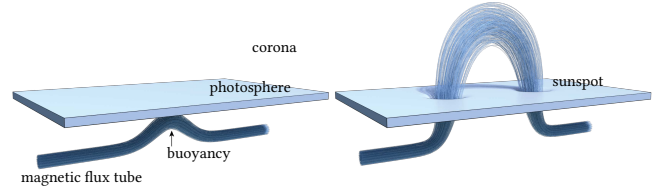
Fig. 3. Left: Below the sun's surface, a strong magnetic field is structured into a bundle of filaments by the convection flow. Right: Buoyancy makes some of these fibers rise above the sun's surface. This is the origin of the fibered structure of the corona.

5 THIN FLUX TUBES

The visually prominent features in the solar atmosphere do not form from processes in the corona itself. Instead, thin *flux tubes*—flux domains with cylindrical boundary—emerge from below the solar surface (Fig. 3) (see also [Priest 2014, Sec. 9.3; Priest 2019, Sec. 3.2]). The pressure in the interior of these flux tubes is lower than the ambient pressure, raising the flux tubes above the solar surface due to buoyancy.

While rising through the photosphere, the flux tube expands due to decreasing ambient gas pressure. By App. C the magnetic field is transported by the same vector field as the gas, hence the amount of gas inside the tube remains unchanged. This leads to further decreasing gas density inside the expanding flux tube leaving the pressure there at only a small fraction of the ambient gas pressure [Winebarger et al. 2008]. This is close to the assumptions of the FFCS model.

5.1 Magnetic Filaments

Consider the situation where the whole flux tube $\mathbb{M}_{\mathbf{B}}$ has the shape of a thin tube with circular cross section around an arclength parametrized curve $\gamma : [0, L] \to \mathbb{M}$ with $\gamma(0), \gamma(L) \in \partial \mathbb{M}$. In this case we refer to γ as the *soul curve* of $\mathbb{M}_{\mathbf{B}}$.

To this shape we assign the unique divergence-free potential field on $\mathbb{M}_{\mathbf{B}}$ that is tangent to the boundary of $\mathbb{M}_{\mathbf{B}}$ and realizes the prescribed flux density on $\mathbb{M}_{\mathbf{B}} \cap \partial \mathbb{M}$ (Neumann problem).

In view of Sec. 4.2.2 this amounts to the assumption that we can neglect twisting of field lines inside the tube.

Because the tube is thin—compared to the curvature of γ and the rate of change in its thickness—we can assume that on each cross section the magnetic field will be approximately orthogonal to the cross section and have constant magnitude $B : [0, L] \to \mathbb{R}$. In this situation, the total flux h through the cross section at $\gamma(s)$ is given by $h = B(s)A(s)$. Therefore the cross-sectional area A and hence

the radius r of the tube is determined by B. We call the pair (γ, B) a *magnetic filament.*

The energy of a magnetic filament is defined by

$$\mathcal{E}(\gamma, B) := h \int_0^L \left(\frac{p}{B} + \frac{B}{2\mu_0} \right) ds \approx \mathcal{E}(\mathbb{M}_{\mathbf{B}}, \mathbf{B}). \tag{8}$$

Among all filaments with a given soul curve the energy (8) is minimized for a specific choice of B:

THEOREM 4. *Let (γ, B) be a magnetic filament. Then under variations which leave the shape of the soul curve fixed, the energy (8) is minimized for $B = \sqrt{2\mu_0 p}$.*

PROOF. First we note that the integrand is convex in B. Taking the derivative with respect to B yields criticality if and only if $-p/B^2 + 1/2\mu_0 = 0$. □

The choice $B = \sqrt{2\mu_0 p}$ corresponds to an optimal radius

$$r_{\mathrm{gas}} = \sqrt{\frac{h}{\pi \sqrt{2\mu_0 p}}} \circ \gamma. \tag{9}$$

The curve γ is called *unobstructed* if the tube around γ with radius r_{gas} is embedded without overlaps.

In this case the energy (8) simplifies to a length measured with respect to a conformally changed metric:

$$\mathcal{E}(\gamma, B) = h \sqrt{\frac{2}{\mu_0}} \int_0^L \sqrt{p} \, ds =: h \mathscr{L}_{\mathrm{gas}}(\gamma). \tag{10}$$

In particular, the magnetohydrostatic energy (8) is critical for geodesics:

THEOREM 5. *Unobstructed magnetic filaments follow geodesics with respect to the conformally changed metric $\frac{2p}{\mu_0} \langle \cdot, \cdot \rangle$.*
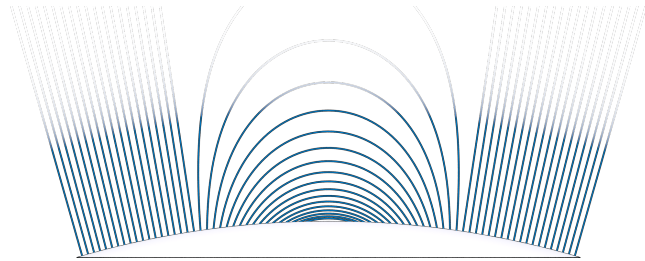
Fig. 4. Unobstructed magnetic filaments follow shortest curves in a certain metric (12). In our solar atmosphere the metric is given by (11) with $\lambda = 23$. Two points whose spherical distance exceeds $2\pi/(\lambda-2)$ are connected by a straight path going out to infinity and back.

5.2 Low Geodesics

In view of Thm. 5 we are interested in the geodesics of the metric $p \langle \cdot, \cdot \rangle$ for a specific choice of pressure function $p: \mathbb{M} \to \mathbb{R}_{>0}$. In this section we derive explicit formulas for these. In the limit of infinite sun radius, these formulas were first given by Low [1982].

5.2.1 Our Solar Atmosphere. Consider a star with radius $r_\odot$ and centered at the origin. For $|\mathbf{x}| \geq r_\odot$ we assume a pressure function of the form

$$p(\mathbf{x}) = p_0 \left(\frac{|\mathbf{x}|}{r_\odot} \right)^{-\lambda}. \tag{11}$$

This choice is in reasonable agreement with measurements [Gent et al. 2013, Fig. 1] while allowing us to give an explicit description for the geodesics of the conformally changed metric

$$d\tilde{s}^2 := p \, ds^2 \tag{12}$$

as used (up to a constant factor) in Eq. (10).

THEOREM 6. *Let $d\tilde{s}^2 := p \, ds^2$, $\theta \in (0, \pi]$ and $\mathbf{x}, \mathbf{y} \in r_\odot \mathbb{S}^2$ be two points on the surface of the sun such that*

$$\mathbf{x} = r_\odot \begin{pmatrix} -\sin \frac{\theta}{2} \\ 0 \\ \cos \frac{\theta}{2} \end{pmatrix}, \quad \mathbf{y} = r_\odot \begin{pmatrix} \sin \frac{\theta}{2} \\ 0 \\ \cos \frac{\theta}{2} \end{pmatrix}.$$

Then the distance between $\mathbf{x}$ and $\mathbf{y}$ measured in $d\tilde{s}$ is

$$d(\mathbf{x}, \mathbf{y}) = \sqrt{p_0} \cdot 2 \sin \left(\min\{\theta, \tfrac{2\pi}{\lambda-2}\} \cdot \tfrac{\lambda-2}{4} \right). \tag{13}$$

Moreover, for $\theta < \frac{2\pi}{\lambda-2}$ the geodesic is given by the map

$$\gamma: \left[-\tfrac{\theta}{2}, \tfrac{\theta}{2} \right] \to \mathbb{M}, \ t \mapsto r_\odot \left(\frac{\cos\left(\frac{\lambda-2}{2} t \right)}{\cos\left(\frac{\lambda-2}{2} \frac{\theta}{2} \right)} \right)^{\frac{2}{\lambda-2}} \begin{pmatrix} \sin t \\ 0 \\ \cos t \end{pmatrix}. \tag{14}$$

For $\theta \geq \frac{2\pi}{\lambda-2}$ the length-minimizing geodesic with respect to $d\tilde{s}$ connecting $\mathbf{x}$ and $\mathbf{y}$ is given by the vertical line going out from $\mathbf{x}$ to infinity followed by the vertical line coming in from infinity to $\mathbf{y}$.

PROOF. See App. E. □

The fact that a geodesic which connects points farther away from one another than $2\pi/(\lambda-2)$ always passes through infinity models *open field lines*—a phenomenon which is also observed in nature.
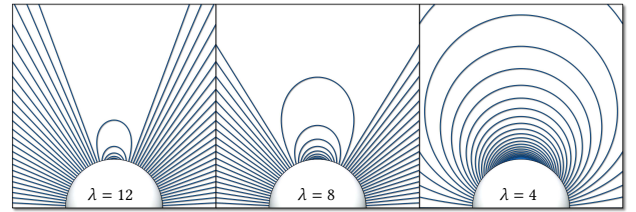
Fig. 5. The λ parameter controls the maximal distance $2\pi/(\lambda-2)$ between points on the sun that can be connected by Low geodesics .

6 ENERGY MINIMIZATION

For the numerical treatment of the FFCS model, we discretize the plasma state $(\mathbb{M}_{\mathbf{B}}, \mathbf{B})$ as a finite collection of magnetic filaments. These filaments are given by a collection Γ of non-intersecting curves: each $\gamma \in \Gamma$ is the soul curve of a magnetic filament whose tube radius at $\gamma(s)$ is given by

$$r_\gamma(s) = \min\{r_{\mathrm{gas}}(s), \tfrac{\mathrm{dist}(s)}{2}\}. \tag{15}$$

Here r_{gas} is given by (9) and dist is the distance to the other curves. The union of the magnetic filaments is used as an approximation for
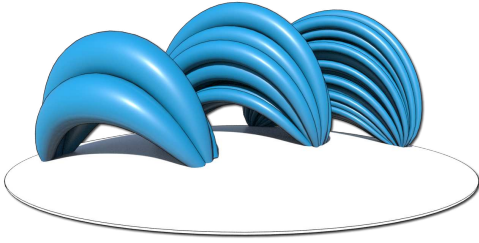

Fig. 6. A flux tube with non-circular cross-section discretized into magnetic filaments, using three different resolutions.

the flux domain $\mathbb{M}_{\mathbf{B}}$ (cf. Fig. 6). As an approximation of the energy $\mathcal{E}(\mathbb{M}_{\mathbf{B}}, \mathbf{B})$ we take the sum of the energies (8) of the individual filaments:

$$\mathcal{E}(\Gamma) = \sum_{\gamma \in \Gamma} h \int_0^{L_\gamma} \left(\frac{p}{B_\gamma} + \frac{B_\gamma}{2\mu_0} \right) ds. \qquad (16)$$

We interpret $B_\gamma = h/(\pi r_\gamma^2)$ as evaluation of the underlying magnetic field strength $|\mathbf{B}|$ and (16) as a discretization of (6).

In view of Thm. 3 we want to approximate FFCS solutions by minimizing (16).
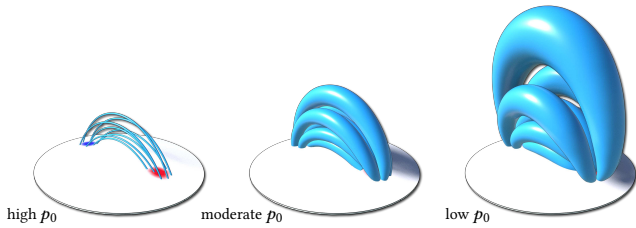
Fig. 7. For the same flux map featuring two isolated sun spots of opposite polarity, we show our computed plasma configurations for different values of the pressure parameter p_0.

6.1 Time-Splitting

The energy (16) is the total length with respect to the conformally changed metric. This metric itself depends on the plasma state approximated by the curve set Γ, and therefore on Γ.

We circumvent the coupled nature of the optimization problem by introducing a time splitting:

First, given a curve configuration, B and hence the conformal factor (7) is computed. Then, assuming the conformal factor is fixed, a gradient descent step is performed. The latter amounts to *curve-shortening flow* (cf. (16)). To find a fixed point, these two steps are alternated until convergence.

Fig. 8 depicts the evolution of the energy over time which is typical for the examples in this paper. The energy minimization progresses rapidly in the early stage of the relaxation and then slowly approaches an equilibrium.

Algorithm 1 Energy Minimization

Input: Initial curve set Γ, pressure decay rate $\lambda > 0$, base pressure $p_0 > 0$.
Output: Γ in relaxed state.
 1: **while** not converged **do**
 2:      $u, \text{grad}\, u \leftarrow \text{COMPUTEMETRIC}(\Gamma)$;   ▷ Sec. F.1.
 3:      $\Gamma \leftarrow \text{CURVESHORTENING}(\Gamma)$;   ▷ Sec. F.2.1.
 4: **end while**
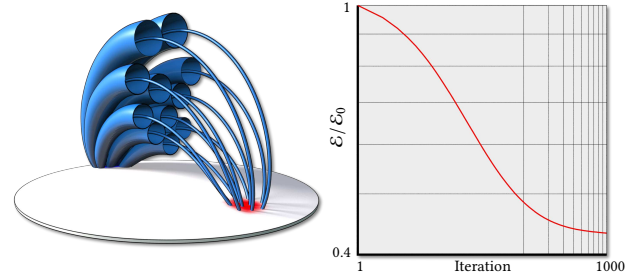
Fig. 8. The graph (right) depicts the energy $\mathcal{E}$ relative to the initial energy $\mathcal{E}_0$ of the configuration as obtained by Alg. 1. The results were obtained for the example of a single sunspot pair (left).

7 INITIAL CURVES FROM FLUX DENSITY

The energy minimization in Sec. 6 requires an initial set of curves which prescribe the field topology. These curves could be designed by an artist or generated procedurally. In this section we describe a method which only requires a flux density map.

First we discretize the flux density on the sun's surface into a finite collection of spots. A common approach is to use pairs of spots with the same strength and opposite polarity [Sheeley et al. 1985; Yeates 2020]. Here we stipple the flux density into many spots with the same absolute flux h. Afterwards we decide which pairs of spots should be joined by a flux tube.

7.1 Stippling the Flux Density

We place entry and exit points of flux on the surface with a density proportional to the prescribed magnetic flux (Fig. 9). A flux-quantization parameter $h > 0$—the strength of each filament—gives rise to $2n$ points $\mathcal{S} \subset \partial\mathbb{M} \cap \partial\mathbb{M}_{\mathbf{B}}$ where

$$n = \left\lceil \frac{1}{2h} \int_{\partial\mathbb{M}} |\Phi| \right\rceil,$$

and $[\cdot]$ indicates rounding. To assure flux-balance, $\mathcal{S}$ must be the union of two disjoint sets $\mathcal{R}$ (red; positive flux), $\mathcal{B}$ (blue; negative flux) of equal cardinality. Our implementation uses the stippling method provided by SideFX Houdini.

7.2 Matching Stipples

Now we must match red and blue base points. In light of (10), energy minimization amounts to minimizing the summed length of
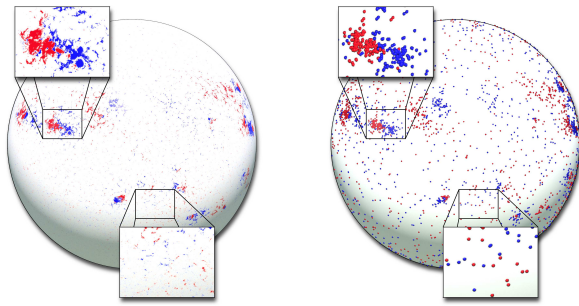
Fig. 9. A stippling (right) of the flux density map from Oct. 21st, 2011 (left).

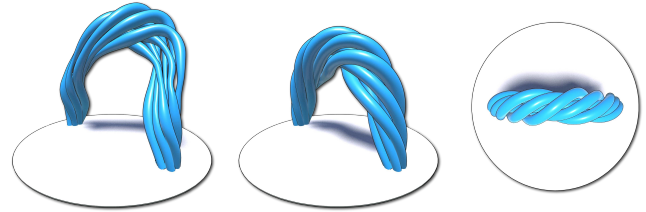Fig. 11. An artistically prescribed collection of initial filaments with 540° twist (left) and the corresponding energy minimizer (middle, right).

filaments in a conformally changed metric. By Sec. 5.2 the distance between matched points in this conformally changed metric depends only on their spherical distance (Eq. (13)). Therefore, finding an energy-minimizing matching of points $\mathcal{M}$ amounts to solving a *linear assignment problem*. Points receive their optimal match within a spherical distance of $2\pi/(\lambda-2)$ or are matched to a virtual point at infinity. Due to this fact, the assignment problem generally becomes sparse and we can use the LAPJVsp algorithm [Jonker and Volgenant 1987] provided by SciPy.

Once the optimal matching has been found, initial curves are constructed according to Eq. (14) (cf. Fig. 10, left).

Fig. 10. Left: A curve configuration initialized from the stippling in Fig. 9 of the flux map of Oct. 21st, 2011. All filaments are vertical plane curves or radial straight line segments. Right: The same configuration in a relaxed state.

8 TWIST

The minimum-energy matching of stipples on the sun's surface by Low-geodesics (Sec. 7.2) results in an untwisted set of initial filaments. It is of course possible (e.g. under artist direction) to start the relaxation with a different set of connecting filaments. For example, one can connect the stipples of a sunspot pair in a twisted fashion (Fig. 11).

Instead of prescribing the twisted connecting curves explicitly, one can also start with the untwisted connections, relax, rotate the sun spots against each other by a small amount, relax again and so on. This is called *quasi-static evolution* and is in fact the mechanism

by which twisted solar loops evolve, see e.g. [Priest 2014, Sec. 1.9] (Fig. 12).
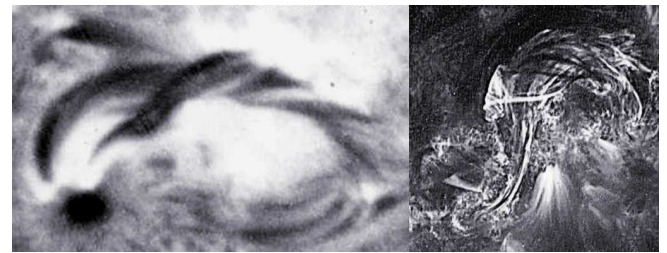
Fig. 12. Twisted flux tubes (courtesy: Crimea Astrophysical Observatory, left and TRACE Consortium, right).

Following the gradient flow of an energy while ignoring inertia effects is called *viscosity dynamics*. When used in connection with boundary conditions or other parameters that change in time the resulting dynamics is referred to as *quasi-static viscosity evolution*, which has been used for modeling plastic elasticity and fracture [Toader and Zanini 2009; Hahn and Wojtan 2015; Negri 2021]. In our context this provides a simple technique for introducing dynamics into simulations (Fig. 13).
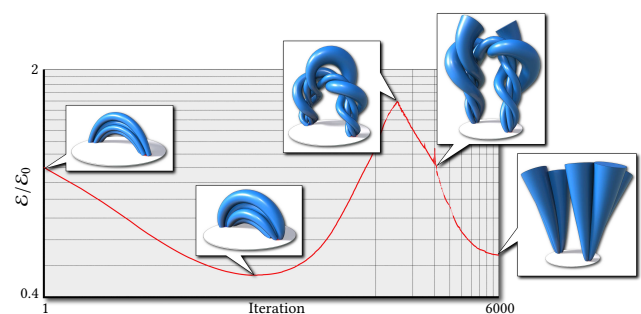
Fig. 13. Time evolution and plot of energy (16) of a *twisted* curve configuration over a single sunspot pair, obtained by moving the base points [Prior and Yeates 2016a,b; Rachmeler et al. 2009]. This can be viewed as a model for a coronal mass ejection: in the twisted state the energy is larger than in the final erupted state—the difference being the amount of energy ejected into space.

9 RENDERING

In order to increase the visual level of detail we can subdivide magnetic filaments into several thinner subfilaments. Since we assume magnetic filaments to be internally untwisted (Sec. 5.1), we are able to guess the shapes of their individual subfilaments.

This subdivision also allows us to model the visible glow by taking into account the small amount of gas trapped between the subfilaments. The glow is determined by the temperature and density of this gas.
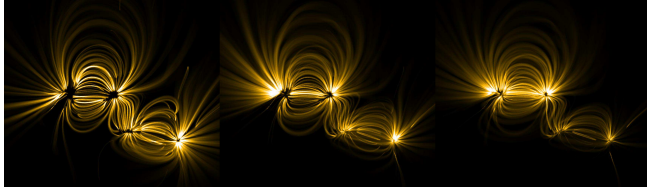

Fig. 14. Glow of an active region from Apr. 19th, 2011 computed for $\rho_0 = 2 \cdot 10^{-8}$ (left), $\rho_0 = 6 \cdot 10^{-8}$ (middle) and $\rho_0 = 1 \cdot 10^{-7}$ (right). The same region was used in [Warren et al. 2018, Fig. 9] and the real footage is shown in the last column of Fig. 17.

9.1 Filament Glow

Let $s \mapsto \gamma(s)$ be the soul curve of a magnetic filament. In plasma, heat transport is weak in directions orthogonal to magnetic field lines but strong parallel to **B**. For this reason and because magnetic filaments are thin (Sec. 5.1), we assume that the temperature of the trapped gas is a constant T_γ throughout the whole filament [Reale 2014; Reale and Peres 1999]. The pressure of this gas is still given by (4) and the ideal gas equation $\rho = mp/(k_B T)$ then gives us the density

$$\rho(s) = \frac{mB(s)^2}{2\mu_0 k_B T_\gamma}.$$

We determine T_γ by assuming that on the sun's surface the density is a given constant ρ_0. If γ is not open, we combine the resulting temperatures at the two end points as

$$T_\gamma = \frac{m}{2\mu_0 k_B \rho_0} \max\{B(0)^2, B(L)^2\}.$$

Solar loops are best seen in extreme ultraviolet and X-ray frequencies. We therefore have to specify the amount of radiation emitted at several wavelengths α.

In the context of a certain fixed density, the emissivity of solar plasma was determined for various common wavelengths α as *temperature response functions* f_α [Boerner et al. 2012, Fig. 11]. Here we need to know also the dependence of emission on density and we found that the following expression leads to good results (Fig. 21):

$$\text{em}(\alpha, T, \rho) = f_\alpha(T)\, \rho^{1/3}.$$

10 VALIDATION

In this section we will separately validate various aspects of our algorithm.

10.1 Validation of the Numerics

Consider the case without gas, i.e. $p = 0$. In simple situations like the one shown in Fig. 15 the energy-minimizing matching described in Sec. 7.2 will yield the same field topology as the corresponding PFSS field. Fig. 15 demonstrates that the soul curves computed by our algorithm are close to the field lines of the PFSS field. We take this as validation for the claim that indeed our numerics approximately yields a force-free field in the interior of the flux domain $\mathbb{M}_\mathbf{B}$.
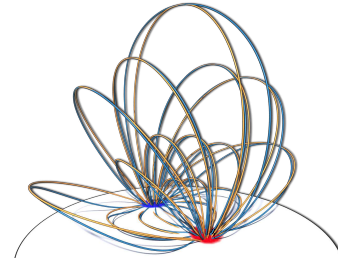

Fig. 15. If the magnetic field is so strong that we can assume $p = 0$, the soul curves of magnetic filaments (blue) computed by our method are close to field lines (yellow) of a PFSS field.

By Thm. 1, the other property of FFCS solutions that has to be verified is that on the boundary of the flux region $\mathbb{M}_B$ the magnetic field strength $|\mathbf{B}|$ is determined by the ambient gas pressure. We tested this in the case $p = \text{const} > 0$ by relaxing a pair of two interlinked flux tori. The cross-sectional area of a filament is inversely proportional to the magnetic field strength inside, so on the boundary $\partial\mathbb{M}_\mathbf{B}$ we expect filaments to have constant thickness. Indeed, Fig. 16 shows that our numerics produces filaments for which this is approximately the case.
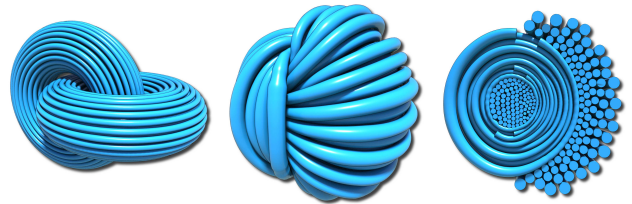

Fig. 16. A pair of linked flux tori (left) relaxed within a constant ambient gas pressure (middle, right).

10.2 Applicability of the FFCS Model

In regions within the solar atmosphere where the magnetic field is strong (like above strong sunspots) the FFCS model predicts a force-free magnetic field. In view of Sec. 4.2.2, in a situation where all field lines are untwisted—as for initial curve configurations obtained from our optimal matching (Sec. 7.2)—we expect a field that is approximately PFSS (Fig. 17).

However, if one also includes the regions with a weak magnetic flux, the field predicted by our model differs significantly from the PFSS field: The PFSS field exhibits long field lines connecting far
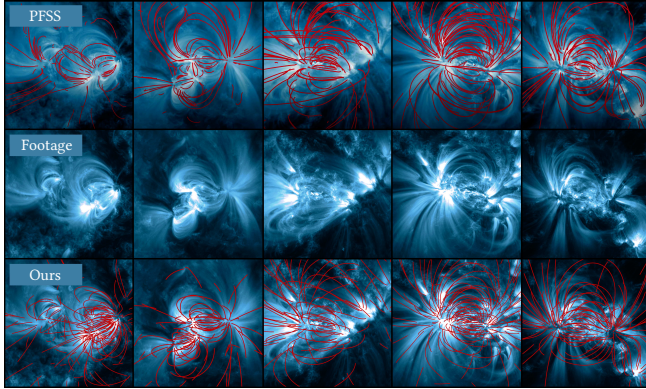
Fig. 17. PFSS field lines [Warren et al. 2018, Fig. 9] (top) compared to our magnetic filaments (bottom).

away points on the surface, while our algorithm produces shallow short filaments (Fig. 18). Since regions with weak magnetic field are less visible in footage, it is hard to verify our predictions visually. However, there are indications that our predictions concerning regions with weak field are indeed realistic [Wiegelmann and Solanki 2004b,a].

Fig. 18. Magnetic field of Oct. 21st, 2011 computed by our method (left) and PFSS (right), both visualized by magnetic filaments.
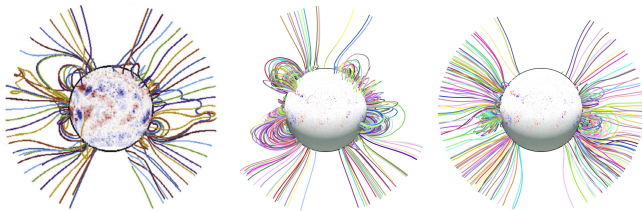
Fig. 19. The far magnetic field during the eclipse on Mar. 15th, 2015 reconstructed by the NLF-OP model (left, from [Yeates et al. 2018, Fig. 7]), the PFSS model (middle) and our model (right).

Also farther away from the sun our field is quite different from the corresponding PFSS field. The far magnetic field of the sun, as reconstructed by various non-PFSS models, was compared in [Yeates

et al. 2018]. In Fig. 19 our field is drawn in the same style, whereas in Fig. 20 we use our glow model (Sec. 9.1) for rendering.
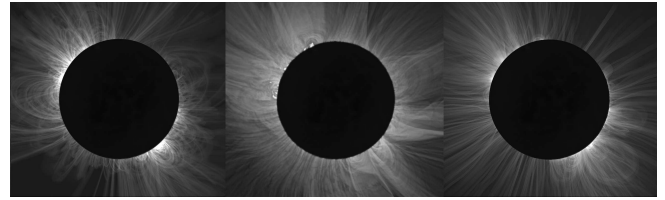
Fig. 20. The far magnetic field (middle, Image by Miroslav Druckmüller, Shadia Habbal, Peter Aniol, Pavel Štarha) during the eclipse on Mar. 15th, 2015 reconstructed and rendered by our model (right) and the PFSS model (left).

10.3 Validation of the Glow Model

Our glow model depends on a single parameter ρ_0 whose effect is illustrated in Fig. 14. Fig. 21 shows footage taken in two different wavelength and the corresponding renderings.
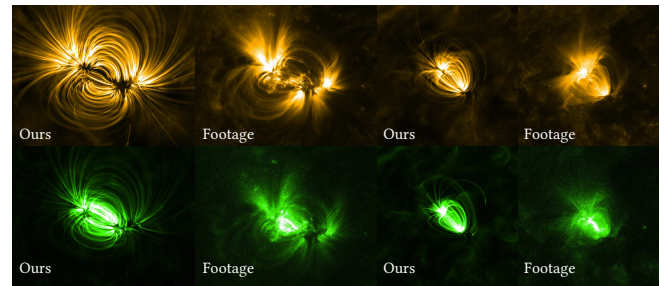

Fig. 21. Comparisons of our output to images of [NASA Solar Dynamics Observatory 2022] in extreme ultraviolet (171Å, yellow) and X-ray (94Å, green). Left half: The region studied in [Williams et al. 2020]. Right half: An active region on Jun. 19th, 2010 (compare [Warren et al. 2018, Fig. 8]).

Given a PFSS field we turn it into a collection of magnetic filaments by tracing field lines from a stippling. The radius of the filaments is given by Eq. (15) with r_{gas} set to infinity (Fig. 18). For rendering (Fig. 20 and Fig. 22, left) one can then apply our glow model.

As explained in Sec. 10.2, in regions with strong magnetic field (which are visually most prominent) the field lines produced by our model are close to the PFSS field lines, resulting in remarkably similar renderings (Fig. 22).

11 CHOOSING PARAMETERS

For the procedural generation of stars one mainly has to specify the parameters λ and p_0. For our sun $\lambda = 23$, $p_0 = 10^{-2}$Pa [Gent et al. 2013, Fig. 1]. For other stars, different choices might be appropriate (Fig. 5, Fig. 7).

In addition, the parameter h controls the quantization of flux maps. It influences level of detail (Fig. 6) and affects computational performance.
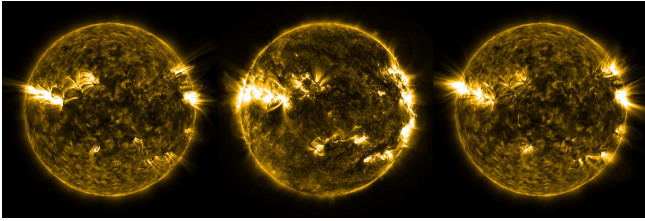
Fig. 22. Real footage of the solar atmosphere on Oct. 21st, 2011 (middle) compared to the output from our rendering method applied on the PFSS model (left) and our algorithm (right) computed from the corresponding frontal flux map (Sec. 10).

For the final rendering we also need to prescribe the gas density ρ_0 inside of the flux ropes at their foot points (Sec. 9.1). For our renderings we use a constant value ranging from 10^{-8} to 10^{-7}.

12 PERFORMANCE AND LIMITATIONS

The computation time of our algorithm ranges depending on the total number of vertices, which is influenced by the flux quantization parameter, the edge length ℓ of discrete curves and the height H at which we clip open field lines.

The resulting number of vertices and computation times when run on a Ryzen 7 5800X CPU are displayed in Table 1. The parameters (normalized by sun radii) we use are $h = 10^{-6}$, $\ell = 0.02$, $H = 0.5$ and 100 iterations. For the close ups on Fig. 21 we increase the level of detail by choosing $h = 5 \cdot 10^{-7}$, $\ell = 0.01$ and 300 iterations.

Table 1. Computation times and parameters for our algorithm. Initialization refers to the combined computation time of stippling, matching and initializing curves. The last column shows the computation time of the energy minimization (Alg. 1).

Application	Vertices	Init.	min $\mathcal{E}$
Fig. 1	≈69k	0.98s	2:04min
Fig. 2	≈66k	2.86s	2:06min
Fig. 22 Ours	≈35k	2.1s	2:36min
Fig. 21 Left half	≈15k	0.073s	13.49s
Fig. 21 Right half	≈3k	0.082s	9.66s

To compute tube radii (cf. Eq. (15)) and the gradient of the logarithmic conformal factor (Sec. F.1.2) at a given vertex we have to find its neighbors. This step accounts for the majority ($\approx 90\%$) of our computation time in Alg. 1. Introducing parallelization, for example through the use of GPU-based neighborhood search [Garcia et al. 2008; Gross et al. 2019] could therefore significantly reduce the overall runtime.

The typical computation times for PFSS fields using *pfsspy* [Stansby et al. 2020] and different magnetogram resolutions are shown in Table 2. Each computation requires a full curvilinear grid around the sun and a radial source surface outer boundary at which the field becomes radial. Here, we set the shell at 2.5 sun radii.

As explained in Sec. 10.3, for renderings based on our glow model, the visible detail is transferred from a magnetogram (possibly with high resolution) on the surface to field lines. Therefore, for rendering

Table 2. Computation times for the PFSS field (*pfsspy* [Stansby et al. 2020]) using data for Oct. 21, 2011 (Fig. 22) with different grid resolutions.

pfsspy resolution	Time
$720 \times 288 \times 50$	8.53s
$1440 \times 576 \times 50$	58.51s
$2160 \times 864 \times 50$	2:16min

the full sun (Fig. 22), even a coarse pfsspy resolution would be sufficient, resulting in a considerably faster computation time compared to ours. For rendering detailed close-ups (Fig. 21), our method is competitive even with regards to computation time (Table 1).

The convergence of our energy minimization (Alg. 1) slows down as we approach a minimum (Fig. 8). It may be possible to avoid this with the use of numerical acceleration techniques [Peng et al. 2018].

For our renderings we use Houdini's *Mantra* renderer. We upsample each flux tube into 50 subfilaments (Sec. 9) which are rendered as transparent curves with an emission shader according to our glow model (Sec. 9.1). The sun surface and fog are subsequently added as composite layers. The total emission per pixel creates a grayscale image, which is then tone-mapped. Rendering time of the glow model depends on the curve details. For all images (1080p) of full suns in our paper it took less than one minute.

While the flux data on the sun's surface varies slowly over time, video footage of the sun shows local changes of filament brightness. These brightness changes are not part of our emission model. In our videos, we include this effect by using animated brightness noise, multiplying all points of a given filament by the same factor.

13 OUTLOOK

In our glow model, we treat the density ρ_0 (Sec. 9.1) as a global constant which can be adapted for each rendering. A method for generating ρ_0 locally from the magnetic field on the surface would be valuable and could improve the fidelity in comparisons with real imagery. We leave this to future work.

Given that our model is based on MHS no dynamic effects are included as of yet. Flow on the sun surface could in principle be accounted for (Fig. 13, Sec. 8). Modeling more general changes of the magnetogram would require a time coherent stippling method [Schrijver and DeRosa 2003]. More refined dynamical models would have to include phenomena such as reconnection of magnetic filaments.

REFERENCES

M. D. Altschuler and G. Newkirk. 1969. Magnetic Fields and the Structure of the Solar Corona. *Sol. Phys.* 9, 1 (1969), 131–149.

A. Angelidis and F. Neyret. 2005. Simulation of Smoke based on Vortex Filament Primitives. In *Proc. Symp. Comp. Anim.* ACM, New York, NY, USA, 87–96.

B. Angles, D. Rebain, M. Macklin, B. Wyvill, L. Barthe, J. P. Lewis, J. von der Pahlen, S. Izadi, J. Valentin, S. Bouaziz, and A. Tagliasacchi. 2019. VIPER: Volume Invariant Position-Based Elastic Rods. *Proc. ACM Comput. Graph. Interact. Tech.* 2, 2 (2019), 19:1–19:26.

M. J. Aschwanden, K. Reardon, and D. B. Jess. 2016. Tracing the Chromospheric and Coronal Magnetic Field with AIA, IRIS, IBIS, and ROSA Data. *Astrophys. J.* 826, 1 (2016), 61.

P. Boerner, C. Edwards, J. Lemen, A. Rausch, C. Schrijver, R. Shine, L. Shing, R. Stern, T. Tarbell, C. J. Wolfson, et al. 2012. Initial Calibration of the Atmospheric Imaging Assembly (AIA) on the Solar Dynamics Observatory (SDO). *Sol. Phys.* 275, 1-2 (2012), 41–66.

K. Borkiewicz, A. J. Christensen, D. Berry, C. Fluke, G. Shirah, and K. Elkins. 2019. Cinematic Scientific Visualization: The Art of Communicating Science. In *SIGGRAPH Asia 2019 Courses*. ACM, New York, NY, USA, Article 107, 313 pages.

CADENS. 2015. *Solar Superstorms*. Centrality of Advanced Digitally ENabled Science.

R. Chodura and A. Schlüter. 1981. A 3D code for MHD Equilibrium and Stability. *J. Comput. Phys.* 41, 1 (1981), 68–88.

C. E. DeForest and C. C. Kankelborg. 2007. Fluxon Modeling of Low-Beta Plasmas. *J. Atmos. Sol.-Terr. Phys.* 69, 1 (2007), 116–128.

V. Garcia, E. Debreuve, and M. Barlaud. 2008. Fast k Nearest Neighbor Search using GPU. In *2008 IEEE Computer Society Conference on Computer Vision and Pattern Recognition Workshops*. IEEE, Anchorage, AK, USA, 1–6.

F. A. Gent, V. Fedun, S. J. Mumford, and R. Erdélyi. 2013. Magnetohydrostatic Equilibrium – I. Three-Dimensional Open Magnetic Flux Tube in the Stratified Solar Atmosphere. *Mon. Notices Royal Astron. Soc.* 435, 1 (2013), 689–697.

J. Gómez, J. Blinn, D. Em, and S. Rueff. 2017. History of the JPL Computer Graphics Lab. ACM SIGGRAPH 2017 Panel.

H. Grad and H. Rubin. 1958. Hydromagnetic Equilibria and Force-Free Fields. *J. nucl. Energy* 7, 3-4 (1958), 284–285.

J. Gross, M. Köster, and A. Krüger. 2019. Fast and Efficient Nearest Neighbor Search for Particle Simulations. In *Computer Graphics and Visual Computing (CGVC)*. The Eurographics Association, 55–63.

S. Hadap and N. Magnenat-Thalmann. 2001. Modeling Dynamic Hair as a Continuum. *Comp. Graph. Forum* 20, 3 (2001), 329–338.

D. Hahn and C. Wojtan. 2015. High-Resolution Brittle Fracture Simulation with Boundary Elements. *ACM Trans. Graph.* 34, 4 (2015), 1–12.

B. Inhester and T. Wiegelmann. 2006. Nonlinear Force-Free Magnetic Field Extrapolations: Comparison of the Grad Rubin and Wheatland Sturrock Roumeliotis Algorithm. *Sol. Phys.* 235, 1 (2006), 201–221.

Å. M. Janse, B. C. Low, and E. N. Parker. 2010. Topological Complexity and Tangential Discontinuity in Magnetic Fields. *Phys. Plasmas.* 17, 9 (2010), 092901.

R. Jonker and A. Volgenant. 1987. A Shortest Augmenting Path Algorithm for Dense and Sparse Linear Assignment Problems. *Comp.* 38, 4 (1987), 325–340.

R. Kippenhahn and A. Schlüter. 1957. Eine Theorie der Solaren Filamente. Mit 7 Textabbildungen. *Z. Astrophys.* 43 (1957), 36–62.

R. Lionello, J. A. Linker, and Z. Mikić. 2008. Multispectral Emission of the Sun During the First Whole Sun Month: Magnetohydrodynamic Simulations. *Astrophys. J.* 690, 1 (2008), 902.

B. C. Low. 1982. Magnetostatic atmospheres with variations in three dimensions. *Astrophys. J.* 263 (1982), 952–969.

G. M. Machado, F. Sadlo, T. Müller, D. Müller, and T. Ertl. 2012. Visualizing Solar Dynamics Data. In *Vision, Modeling and Visualization*. The Eurographics Association, 95–102.

H. Moradi, C. Baldner, A. C. Birch, D. C. Braun, R. H. Cameron, T. L. Duvall, L. Gizon, D. Haber, S. M. Hanasoge, B. W. Hindman, J. Jackiewicz, E. Khomenko, R. Komm, P. Rajaguru, M. Rempel, M. Roth, R. Schlichenmaier, H. Schunker, H. C. Spruit, K. G. Strassmeier, M. J. Thompson, and S. Zharkov. 2010. Modeling the Subsurface Structure of Sunspots. *Sol. Phys.* 267, 1 (2010), 1–62.

M. S. Nabizadeh, A. Chern, and R. Ramamoorthi. 2021. Kelvin Transformations for Simulations on Infinite Domains. *ACM Trans. Graph.* 40, 4 (2021), 97:1–97:15.

J. P. Naiman, K. Borkiewicz, and A. J. Christensen. 2017. Houdini for Astrophysical Visualization. *Publ. Astron. Soc. Pac.* 129, 975 (2017), 058008.

NASA Scientific Visualization Studio. 2018. The Dynamic Solar Magnetic Field with Introduction.

NASA Solar Dynamics Observatory. 2022. NASA AIA/HMI Data.

M. Negri. 2021. A Quasi-Static Model for Craquelure Patterns. In *Mathematical Modeling in Cultural Heritage*. Springer, Cham, 147–164.

M. Padilla, A. Chern, F. Knöppel, U. Pinkall, and P. Schröder. 2019. On Bubble Rings and Ink Chandeliers. *ACM Trans. Graph.* 38, 4 (2019), 129:1–129:14.

E. N. Parker. 1994. *Spontaneous Current Sheets in Magnetic Fields: With Applications to Stellar X-Rays.* Vol. 1. Ox. U. P., New York, NY.

Y. Peng, B. Deng, J. Zhang, F. Geng, W. Qin, and L. Liu. 2018. Anderson Acceleration for Geometry Optimization and Physics Simulation. *ACM Trans. Graph.* 37, 4 (2018), 42:1–42:14.

H. Peter, S. Bingert, and S. Kamio. 2012. Catastrophic Cooling and Cessation of Heating in the Solar Corona. *Astron. Astrophys.* 537 (2012), A152.

E. R. Priest. 2014. *Magnetohydrodynamics of the Sun.* Cam. U. P.

E. R. Priest. 2019. Magnetohydrodynamics and Solar Dynamo Action. In *The Sun as a Guide to Stellar Physics.* Elsevier, 239–266.

C. Prior and A. R. Yeates. 2016a. Twisted Versus Braided Magnetic Flux Ropes in Coronal Geometry – I. Construction and Relaxation. *Astron. Astrophys.* 587 (2016), 15.

C. Prior and A. R. Yeates. 2016b. Twisted Versus Braided Magnetic Flux Ropes in Coronal Geometry – II. Comparative Behaviour. *Astron. Astrophys.* 591 (2016), 20.

L. A. Rachmeler, C. E. DeForest, and C. C. Kankelborg. 2009. Reconnectionless CME Eruption: Putting the Aly-Sturrock Conjecture to Rest. *Astrophys. J.* 693, 2 (2009), 1431–1436.

F. Reale. 2014. Coronal Loops: Observations and Modeling of Confined Plasma. *Living Rev. Sol. Phys.* 11, 1 (2014), 1–94.

F. Reale and G. Peres. 1999. TRACE-Derived Temperature and Emission Measure Profiles along Long-Lived Coronal Loops: The Role of Filamentation. *Astrophys. J. Lett.* 528, 1 (1999), L45.

M. Reddiger and B. Poirier. 2020. On the Differentiation Lemma and the Reynolds Transport Theorem for Manifolds with Corners. arXiv:1906.03330 [math-ph]

R. Rosner, W. H. Tucker, and G. S. Vaiana. 1978. Dynamics of the Quiescent Solar Corona. *Astrophys. J.* 220 (1978), 643–645.

T. Sakurai. 1982. Green's Function Methods for Potential Magnetic Fields. *Sol. Phys.* 76, 2 (1982), 301–321.

C. J. Schrijver and M. L. DeRosa. 2003. Photospheric and Heliospheric Magnetic Fields. *Solar Physics* 212, 1 (2003), 165–200.

C. J. Schrijver, A. W. Sandman, M. J. Aschwanden, and M. L. De Rosa. 2005. Coronal Heating and the Appearance of Solar and Stellar Coronae. In *13th Cambridge Workshop on Cool Stars, Stellar Systems and the Sun*, Vol. 560. European Space Agency, 65.

N. R. Sheeley, C. R. DeVore, and J. P. Boris. 1985. Simulations of the Mean Solar Magnetic Field During Sunspot Cycle 21. *Sol. Phys.* 98, 2 (1985), 219–239.

D. Stansby, A. R. Yeates, and S. T. Badman. 2020. pfsspy: A Python Package for Potential Field Source Surface Modelling. *J. Open Source Softw.* 5, 54 (2020), 2732.

V. S. Titov, C. Downs, Z. Mikić, T. Török, J. A. Linker, and R. M. Caplan. 2018. Regularized Biot–Savart Laws for Modeling Magnetic Flux Ropes. *Astrophys. J. Lett.* 852, 2 (2018), L21.

R. Toader and C. Zanini. 2009. An Artificial Viscosity Approach to Quasistatic Crack Growth. *Bolletino dell Unione Mat. Ital.* 2, 1 (2009), 1–35.

H. P. Warren, N. A. Crump, I. Ugarte-Urra, X. Sun, M. J. Aschwanden, and T. Wiegelmann. 2018. Toward a Quantitative Comparison of Magnetic Field Extrapolations and Observed Coronal Loops. *Astrophys. J.* 860, 1 (2018), 46.

S. Weißmann and U. Pinkall. 2010. Filament-based Smoke with Vortex Shedding and Variational Reconnection. *ACM Trans. Graph.* 29, 4 (2010), 115:1–12.

T. Wiegelmann and S. K. Solanki. 2004a. Similarities and Differences between Coronal Holes and the Quiet Sun: Are Loop Statistics the Key? *Sol. Phys.* 225, 2 (2004), 227–247.

T. Wiegelmann and S. K. Solanki. 2004b. Why Are Coronal Holes Indistinguishable from the Quiet Sun in Transition Region Radiation?. In *SOHO 15 Coronal Heating*, Vol. 575. European Space Agency, 35.

T. Williams, R. W. Walsh, A. R. Winebarger, D. H. Brooks, J. W. Cirtain, B. De Pontieu, L. Golub, K. Kobayashi, D. E. McKenzie, R. J. Morton, H. Peter, L. A. Rachmeler, S. L. Savage, P. Testa, S. K. Tiwari, H. P. Warren, and B. J. Watkinson. 2020. Is the High-Resolution Coronal Imager Resolving Coronal Strands? Results from AR 12712. *Astrophys. J.* 892, 2 (2020), 134.

A. R. Winebarger, H. P. Warren, and D. A. Falconer. 2008. Modeling X-Ray Loops and EUV "Moss" in an Active Region Core. *Astrophys. J.* 676, 1 (2008), 672.

A. R. Yeates. 2020. How Good is the Bipolar Approximation of Active Regions for Surface Flux Transport? *Sol. Phys.* 295, 9 (2020), 119.

A. R. Yeates, T. Amari, I. Contopoulos, X. Feng, D. H. Mackay, Z. Mikić, T. Wiegelmann, J. Hutton, C. A. Lowder, H. Morgan, et al. 2018. Global Non-Potential Magnetic Models of the Solar Corona During the March 2015 Eclipse. *Space Sci. Rev.* 214, 5 (2018), 99.

C. Yu, H. Schumacher, and K. Crane. 2021. Repulsive Curves. *ACM Trans. Graph.* 40, 2 (2021), 268:1–268:19.

J. Zhuleku, J. Warnecke, and H. Peter. 2020. Stellar Coronal X-ray Emission and Surface Magnetic Flux. *Astron. Astrophys.* 640 (2020), A119.

NOTATIONS

Notation	Meaning
$\mathbb{M}$	Exterior of the sun
$\partial\mathbb{M}$	Sun surface
$\mathbb{M}_{\mathbf{0}}$	Gas domain
$\mathbb{M}_{\mathbf{B}}$	Flux domain
$\Sigma_{\mathbf{B}}$	Flux regions on the sun surface
$\mathbf{B}$	Magnetic field
k_{B}	Boltzmann constant
μ_0	Permeability of the vacuum
m	Mass of the proton
p	Pressure
ρ	Density
$r_\odot$	Radius of the sun
T	Temperature
u	Logarithmic conformal factor
h	Flux quantization parameter
λ	Pressure decay rate
ds	Euclidean length element
$d\tilde{s}$	Conformally changed length element
Φ	Flux density
$\mathcal{S}$	Stippling of the flux density Φ
$\mathcal{R}$	Red stipples for positive flux
$\mathcal{B}$	Blue stipples for negative flux
$\mathcal{M}$	Matching of stipples

A EXTENSION OF THE PRESSURE FUNCTION

THEOREM 7. *With the sun of radius $r_\odot$ and centered at the origin, suppose that $\{\mathbf{x} \in \mathbb{M}_{\mathbf{0}} \mid |\mathbf{x}| = r\}$ is connected for all $r \geq r_\odot$. Then, for a function $f\colon [r_\odot, \infty) \to \mathbb{R}_{>0}$, the gas pressure p_{gas} is of the form*

$$p_{gas} = p|_{\mathbb{M}_{\mathbf{0}}},$$

where $p\colon \mathbb{M} \to \mathbb{R}_{>0}$ with $p(\mathbf{x}) = f(|\mathbf{x}|)$.

PROOF. Since the force of gravity is radial, by Eq. (1) $\operatorname{grad} p_{gas}$ is as well. Hence the level sets of p lie on concentric spheres. The extension is then obtained by extending these level sets to the whole of the concentric spheres. □

B PROOF OF THM. 1

To prove the claim we express $\mathbf{B}$ and p_{gas} as the limit of a smooth magnetic field $\tilde{\mathbf{B}}$ and a smooth gas pressure $\tilde{p}$. Therefore, let $\varepsilon > 0$ be small and let $\mathbb{M}_{\mathbf{0}}^\varepsilon$ denote the ε-neighborhood of $\mathbb{M}_{\mathbf{0}}$. Now, let $\varphi_{\mathbf{B}}, \varphi_{\mathbf{0}}\colon \mathbb{M} \to [0,1]$ be smooth functions such that

$$\varphi_{\mathbf{B}}|_{\mathbb{M}_{\mathbf{B}}\setminus\mathbb{M}_{\mathbf{0}}^\varepsilon} = 1, \quad \varphi_{\mathbf{B}}|_{\mathbb{M}_{\mathbf{0}}} = 0, \quad \varphi_{\mathbf{0}}|_{\mathbb{M}_{\mathbf{0}}} = 1, \quad \varphi_{\mathbf{0}}|_{\mathbb{M}_{\mathbf{B}}\setminus\mathbb{M}_{\mathbf{0}}^\varepsilon} = 0$$

and define

$$\tilde{\mathbf{B}} = \varphi_{\mathbf{B}}\mathbf{B}, \quad \tilde{p} = \varphi_{\mathbf{0}}p,$$

where p is the extension of the gas pressure function in Thm. 7. In particular, we have

$$\operatorname{curl}\tilde{\mathbf{B}} = \varphi_{\mathbf{B}}\operatorname{curl}\mathbf{B} + \operatorname{grad}\varphi_{\mathbf{B}} \times \mathbf{B}$$

and

$$\begin{aligned}
(\operatorname{curl}\tilde{\mathbf{B}}) \times \tilde{\mathbf{B}} &= \varphi_{\mathbf{B}}^2 \operatorname{curl}\mathbf{B} \times \mathbf{B} + \tfrac{1}{2}(\operatorname{grad}\varphi_{\mathbf{B}}^2 \times \mathbf{B}) \times \mathbf{B} \\
&= \varphi_{\mathbf{B}}^2\operatorname{curl}\mathbf{B} \times \mathbf{B} + \tfrac{1}{2}(\mathbf{B}\langle\operatorname{grad}\varphi_{\mathbf{B}}^2, \mathbf{B}\rangle - \operatorname{grad}\varphi_{\mathbf{B}}^2|\mathbf{B}|^2).
\end{aligned}$$

Now, let Y be a vector field compactly supported away from the boundary $\partial\mathbb{M}$. Then, for $\varepsilon \to 0$, we get, using Stokes' Theorem

$$\begin{aligned}
\int_{\mathbb{M}}\langle(\operatorname{curl}\tilde{\mathbf{B}}) &\times \tilde{\mathbf{B}}, Y\rangle - \int_{\mathbb{M}_{\mathbf{B}}}\langle(\operatorname{curl}\mathbf{B}) \times \mathbf{B}, Y\rangle \\
&= \tfrac{1}{2}\int_{\mathbb{M}}\langle\operatorname{grad}\varphi_{\mathbf{B}}^2, \langle\mathbf{B}, Y\rangle\mathbf{B} - |\mathbf{B}|^2 Y\rangle + o(1) \\
&= -\tfrac{1}{2}\int_{\mathbb{M}_{\mathbf{B}}}\operatorname{div}(\langle\mathbf{B}, Y\rangle\mathbf{B} - |\mathbf{B}|^2 Y) + o(1) \\
&= \tfrac{1}{2}\int_{\partial\mathbb{M}_{\mathbf{B}}}|\mathbf{B}|^2\langle Y, N\rangle + o(1).
\end{aligned}$$

Here in the last equation we used that the normal unit vector N of $\partial\mathbb{M}_{\mathbf{B}}$ and $\mathbf{B}$ are perpendicular, $N \perp \mathbf{B}|_{\partial\mathbb{M}_{\mathbf{B}}}$. Similarly,

$$\begin{aligned}
\int_{\mathbb{M}}\langle\operatorname{grad}\tilde{p}, Y\rangle &= \int_{\mathbb{M}}\langle p\operatorname{grad}\varphi_{\mathbf{0}} + \varphi_{\mathbf{0}}\operatorname{grad}p, Y\rangle \\
&= \int_{\mathbb{M}}\langle\operatorname{grad}\varphi_{\mathbf{0}}, pY\rangle + \int_{\mathbb{M}_{\mathbf{0}}}\langle\operatorname{grad}p, Y\rangle + o(1) \\
&= -\int_{\mathbb{M}_{\mathbf{0}}}\operatorname{div}(p_{gas}Y) + \int_{\mathbb{M}_{\mathbf{0}}}\langle\operatorname{grad}p_{gas}, Y\rangle + o(1) \\
&= \int_{\partial\mathbb{M}_{\mathbf{B}}}p_{gas}\langle Y, N\rangle + \int_{\mathbb{M}_{\mathbf{0}}}\langle\operatorname{grad}p_{gas}, Y\rangle + o(1).
\end{aligned}$$

Altogether, this shows that

$$\begin{aligned}
\int_{\mathbb{M}}\langle\tfrac{1}{\mu_0}&(\operatorname{curl}\tilde{\mathbf{B}}) \times \tilde{\mathbf{B}} - \operatorname{grad}\tilde{p} + \tfrac{m}{k_B T}\tilde{p}\mathbf{g}, Y\rangle \\
&= \tfrac{1}{\mu_0}\int_{\mathbb{M}_{\mathbf{B}}}\langle(\operatorname{curl}\mathbf{B}) \times \mathbf{B}, Y\rangle + \int_{\mathbb{M}_{\mathbf{0}}}\langle\tfrac{m}{k_B T}p_{gas}\mathbf{g} - \operatorname{grad}p_{gas}, Y\rangle \\
&\quad + \int_{\partial\mathbb{M}_{\mathbf{B}}}(\tfrac{|\mathbf{B}|^2}{2\mu_0} - p_{gas})\langle Y, N\rangle + o(1),
\end{aligned}$$

which tends to zero for arbitrary Y if and only if $(\operatorname{curl}\mathbf{B}) \times \mathbf{B} = 0$, i.e. $\mathbf{B}$ is force-free, on $\mathbb{M}_{\mathbf{B}}$ and $\frac{|\mathbf{B}|^2}{2\mu_0} = p_{gas}$ on $\partial\mathbb{M}_{\mathbf{B}} \cap \partial\mathbb{M}_{\mathbf{0}}$.

C THE MAGNETIC FIELD IS FROZEN IN THE GAS

Let $\mathbb{M}$ be a domain filled by plasma moving under the influence of arbitrary forces. The motion of the gas can be described by a family of diffeomorphisms $t \mapsto \varphi_t\colon \mathbb{M} \to \mathbb{M}$, $t \in (-\epsilon, \epsilon)$ with $\varphi_0 = \operatorname{id}_{\mathbb{M}}$ and velocity field $\mathbf{v} = \frac{\partial}{\partial t}\big|_{t=0}\varphi_t = \mathring{\varphi}$. Then one of the equations of Magnetohydrodynamics says

$$\mathring{B} = \operatorname{curl}(\mathbf{v} \times \mathbf{B}).$$

In terms of $\beta_t = \iota_{B_t}\det$, which satisfies $d\beta_t = 0$, this equation can be written as

$$\mathring{\beta} = -\mathcal{L}_{\mathbf{v}}\beta = -d(\iota_{\mathbf{v}}\beta) - \iota_{\mathbf{v}}(d\beta) = -d(\iota_{\mathbf{v}}\iota_{\mathbf{B}}\det) = \iota_{\operatorname{curl}(\mathbf{B}\times\mathbf{v})}\det,$$

where we use Cartan's magic formula. This implies

$$\beta_t = (\varphi_t^{-1})^* \beta_0.$$

If we visualize a magnetic field as a collection of field lines whose density indicates the field strength, this means that we only have to apply the diffeomorphisms φ_t to these field lines. We conclude: the only variations of a plasma state $(\mathbb{M}_\mathbf{B}, \mathbf{B})$ compatible with the laws of magnetohydrodynamics are those that come from diffeomorphisms of $\mathbb{M}$.
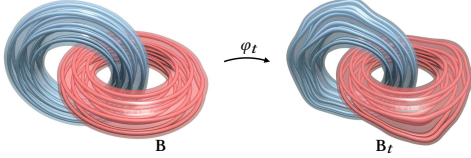

Fig. 23. A magnetic field is transported by transporting its field lines.

D PROOF OF THM. 2

The change in the pressure contribution to the energy is given by

$$\frac{d}{dt}\Big|_{t=0} \int_{\mathbb{M}_\mathbf{B}} \varphi_t^* p = \int_{\mathbb{M}_\mathbf{B}} \mathcal{L}_Y p$$
$$= \int_{\mathbb{M}_\mathbf{B}} \langle \mathrm{grad}\, p, Y \rangle + \int_{\mathbb{M}_\mathbf{B}} p\, \mathrm{div}(Y)$$
$$= \int_{\mathbb{M}_\mathbf{B}} \mathrm{div}(pY)$$
$$= \int_{\partial\mathbb{M}_\mathbf{B}} p \langle Y, N \rangle,$$

where we used Cartan's magic formula, integration by parts and the Divergence theorem.

The time derivative of the magnetic energy is calculated similarly, but we have to keep in mind that instead of the time-independent integrand $p \det$ we now are dealing with a time-dependent integrand $\frac{|\mathbf{B}|^2}{2\mu_0} \det$ and by *Reynolds transport theorem* [Reddiger and Poirier 2020] we get an additional term:

$$\frac{d}{dt}\Big|_{t=0} \int_{\mathbb{M}_\mathbf{B}} \varphi_t^* \left(\frac{|\mathbf{B}|^2}{2\mu_0} \right) = \int_{\mathbb{M}_\mathbf{B}} \frac{1}{\mu_0} \langle \mathring{\mathbf{B}}, \mathbf{B} \rangle + \int_{\partial\mathbb{M}_\mathbf{B}} \frac{|\mathbf{B}|^2}{2\mu_0} \langle Y, N \rangle.$$

For the first summand we compute

$$\int_{\mathbb{M}_\mathbf{B}} \frac{1}{\mu_0} \langle \mathring{\mathbf{B}}, \mathbf{B} \rangle = \int_{\mathbb{M}_\mathbf{B}} \frac{1}{\mu_0} \langle \mathrm{curl}(Y \times \mathbf{B}), \mathbf{B} \rangle$$
$$= \int_{\mathbb{M}_\mathbf{B}} \frac{1}{\mu_0} \langle Y \times \mathbf{B}, \mathrm{curl}\, \mathbf{B} \rangle$$
$$\quad - \int_{\mathbb{M}_\mathbf{B}} \frac{1}{\mu_0} \mathrm{div}(|\mathbf{B}|^2 Y - \langle \mathbf{B}, Y \rangle \mathbf{B})$$
$$= - \int_{\mathbb{M}_\mathbf{B}} \langle \frac{1}{\mu_0} \mathrm{curl}\, \mathbf{B} \times \mathbf{B}, Y \rangle$$
$$\quad - \int_{\partial\mathbb{M}_\mathbf{B}} \left(\frac{|\mathbf{B}|^2}{\mu_0} \langle Y, N \rangle - \frac{1}{\mu_0} \langle \mathbf{B}, Y \rangle \langle \mathbf{B}, N \rangle \right)$$

Putting everything together we obtain

$$\mathring{\mathcal{E}} = - \int_{\mathbb{M}_\mathbf{B}} \langle \frac{1}{\mu_0} \mathrm{curl}\, \mathbf{B} \times \mathbf{B}, Y \rangle$$
$$+ \int_{\partial\mathbb{M}_\mathbf{B}} \left(\left(p - \frac{|\mathbf{B}_j|^2}{2\mu_0} \right) \langle Y, N \rangle + \frac{1}{\mu_0} \langle \mathbf{B}, Y \rangle \langle \mathbf{B}, N \rangle \right).$$

Note that the latter summand of the boundary integral vanishes for variations which fix the boundary $\Sigma_\mathbf{B}$.

E PROOF OF THM. 6

For symmetry reasons, the geodesic in question has to lie in the xz-plane. Denoting $\mathbb{M}_{x,z} := \mathbb{M} \cap \mathrm{span}\{e_x, e_z\}$ and introducing polar coordinates (r, ϕ) on $\mathbb{M}_{x,z}$ we can use the transformation

$$f: \mathbb{M}_{x,z} \to \mathbb{R}^2, \ r \begin{pmatrix} \sin\phi \\ 0 \\ \cos\phi \end{pmatrix} \mapsto \left(\frac{r}{r_\odot} \right)^{-\frac{\lambda-2}{2}} \begin{pmatrix} \sin\left(\frac{\lambda-2}{2}\phi \right) \\ \cos\left(\frac{\lambda-2}{2}\phi \right) \end{pmatrix} \quad (17)$$

in order to map $\mathbb{M}_{x,z}$ onto the interior of the unit disk in $\mathbb{R}^2$. From

$$|df|^2 = \frac{|\lambda-2|^2}{2p_0 r_\odot^{\lambda-2}} p_0 r^{-\lambda} (dr^2 + r^2 d\phi^2) = \frac{|\lambda-2|^2}{2p_0 r_\odot^{\lambda-2}} p_0 r^{-\lambda} |ds|^2$$

we see that the pullback under f of the Euclidean metric on the unit disk is a constant multiple of our conformally changed metric $p_0 (r/r_\odot)^{-\lambda} ds^2$ and therefore the image of a geodesic under f is a geodesic in the unit disk, i.e. a straight line segment (cf. Fig. 24). The map f takes the points $\mathbf{x}$ and $\mathbf{y}$ to

$$\tilde{\mathbf{x}} = \begin{pmatrix} -\sin\left(\frac{\lambda-2}{2} \frac{\theta}{2} \right) \\ \cos\left(\frac{\lambda-2}{2} \frac{\theta}{2} \right) \end{pmatrix} \quad \text{and} \quad \tilde{\mathbf{y}} = \begin{pmatrix} \sin\left(\frac{\lambda-2}{2} \frac{\theta}{2} \right) \\ \cos\left(\frac{\lambda-2}{2} \frac{\theta}{2} \right) \end{pmatrix}.$$

The straight line segment connecting $\tilde{\mathbf{x}}$ to $\tilde{\mathbf{y}}$ can be parametrized by
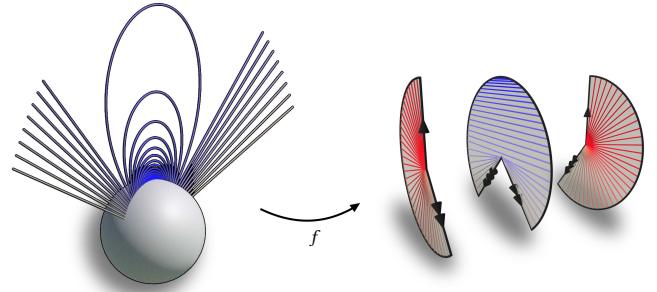

Fig. 24. The map f from Eq. (17) which maps geodesics contained in a plane on the sun's exterior to geodesics in a multiple cover of the unit disc in $\mathbb{R}^2$.

$$\left[-\frac{\theta}{2}, \frac{\theta}{2} \right] \to \mathbb{R}^2, \ t \mapsto \frac{\cos\left(\frac{\lambda-2}{2} \frac{\theta}{2} \right)}{\cos\left(\frac{\lambda-2}{2} t \right)} \begin{pmatrix} \sin\left(\frac{\lambda-2}{2} t \right) \\ \cos\left(\frac{\lambda-2}{2} t \right) \end{pmatrix}.$$

If $\theta < \frac{2\pi}{\lambda-2}$, the geodesic we are looking for is obtained from this straight line segment by applying the inverse of the map f. For $\theta \geq \frac{2\pi}{\lambda-2}$ we have to consider that the map f multiplies angles by a factor of $\frac{\lambda-2}{2} > 1$, so the conformally changed metric on the intersection of the exterior of the sun with the xz-plane has a cone point at infinity. Away from the cone singularity, the metric is flat. However, as it is familiar from triangle meshes, there is negative curvature concentrated in the cone point and as a consequence, many length-minimizing geodesics are forced to pass through the cone point.
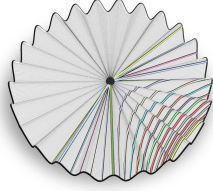
F IMPLEMENTATION

We have implemented our proposed algorithm in SideFX Houdini and the code is available in the supplementary material. For stippling and matching we take advantage of readily available software. Only the minimization of the variational energy (16) requires custom code (Alg. 1).

For the implementation we have to move away from the smooth theory and deal with a configuration of discrete curves. A *discrete curve* is a map $\gamma \colon \{0, \ldots, n\} \to \mathbb{R}^3$ and we denote the position of vertex i by γ_i.

F.1 Logarithmic Conformal Factor and its Gradient

For our purposes we need the logarithmic conformal factor u and its gradient at the vertex positions of the discrete curve γ (cf. Alg. 1 Step 2). Inside the flux domain $\mathbb{M}_\mathbf{B}$, from the factorization introduced in (7), we can write

$$\left(\frac{p}{B} + \frac{B}{2\mu_0}\right) = \sqrt{\frac{2p}{\mu_0}}\left(1 + \frac{(B-\sqrt{2\mu_0 p})^2}{2B\sqrt{2\mu_0 p}}\right) =: e^{u_0}e^{u_{\mathrm{ex}}}.$$

Here u_0 and u_{ex} are the logarithmic conformal factors corresponding to the gas pressure and the pressure-excess factor respectively. Therefore, the logarithmic conformal factor u is of the form

$$u = u_0 + u_{\mathrm{ex}}$$

and consequently

$$\mathrm{grad}\, u = \mathrm{grad}\, u_0 + \mathrm{grad}\, u_{\mathrm{ex}}. \tag{18}$$

F.1.1 Determining the Logarithmic Conformal Factor. We assume the pressure p to be a given function, so that u_0 is known. In the case of (11) we have

$$u_0(\mathbf{x}) = -\frac{\lambda}{2}\log(|\mathbf{x}|) + \log\left(\sqrt{\frac{2p_0}{\mu_0}}\right). \tag{19}$$

Moreover, at a vertex γ_i, we have the cross-sectional area A_i from (15). Hence, from $h = B_i A_i$ and (11), we can compute

$$(u_{\mathrm{ex}})_i = \log\left(1 + \frac{\left(B_i - \sqrt{2\mu_0 p(\gamma_i)}\right)^2}{2B_i\sqrt{2\mu_0 p(\gamma_i)}}\right). \tag{20}$$

F.1.2 Gradient Computation. With (19) we compute the first summand of (18) as

$$(\mathrm{grad}\, u_0)(\mathbf{x}) = -\frac{\lambda}{2}\frac{\mathbf{x}}{|\mathbf{x}|^2}.$$

We approximate $(\mathrm{grad}\, u_{\mathrm{ex}})_i$ from samples, employing a finite difference scheme, evaluating it on the curves only

$$(\mathrm{grad}\, u_{\mathrm{ex}})_i \approx \frac{1}{|\mathcal{N}(\gamma_i)|}\sum_{\gamma_j \in \mathcal{N}(\gamma_i)}\left((u_{\mathrm{ex}})_j - (u_{\mathrm{ex}})_i\right)\frac{\gamma_j - \gamma_i}{|\gamma_j - \gamma_i|^2}.$$

Here $\mathcal{N}(\gamma_i)$ is a set of neighboring vertices of γ_i which we use for sampling, including vertices coming from virtual filaments that fill the gas domain with field strength as in Thm. 4.

F.2 Discrete Curve Shortening

For curve shortening we need the gradient of the conformal length (8).

Let $u \colon \mathbb{R}^3 \to \mathbb{R}$ be a logarithmic conformal factor. The *discrete conformal distance* between two points $\mathbf{x}, \mathbf{y} \in \mathbb{R}^3$ is given by

$$d_u(\mathbf{x}, \mathbf{y}) := e^{\frac{u(\mathbf{x})+u(\mathbf{y})}{2}}|\mathbf{x} - \mathbf{y}|$$

approximates the geodesic distance as $|\mathbf{x} - \mathbf{y}| \to 0$.

The discrete analog of the conformal length (8) for γ is

$$\mathcal{L}(\gamma) = \sum_{i=0}^{n-1} d_u(\gamma_i, \gamma_{i+1}). \tag{21}$$

Consequently, the gradient of (21) with respect to the Euclidean metric at position γ_i can be computed as

$$\begin{aligned}(\mathrm{grad}\,\mathcal{L})_i = {}&\tfrac{1}{2}\left(d_u(\gamma_{i-1}, \gamma_i) + d_u(\gamma_i, \gamma_{i+1})\right)(\mathrm{grad}\, u)(\gamma_i)\\&+ e^{\frac{u(\gamma_{i-1})+u(\gamma_i)}{2}}\frac{\gamma_i - \gamma_{i-1}}{|\gamma_i - \gamma_{i-1}|}\\&- e^{\frac{u(\gamma_i)+u(\gamma_{i+1})}{2}}\frac{\gamma_{i+1} - \gamma_i}{|\gamma_{i+1} - \gamma_i|}.\end{aligned} \tag{22}$$

Here $\mathrm{grad}\, u \colon \mathbb{R}^3 \to \mathbb{R}^3$ is the gradient of u with respect to the Euclidean metric.

From (22) we now develop a finite-difference scheme to minimize the length $\mathcal{L}$.

F.2.1 Curve-Shortening Step. In order to perform the curve-shortening we found updates relying on a quasi-Newton step to work best for our purposes: Denoting the k-th iterate of γ_i by γ_i^k, we use

$$\gamma_i^{k+1} = w_+\gamma_{i+1}^k + w_-\gamma_{i-1}^k - \tfrac{1}{2}\left(w_-\ell_-^2 + w_+\ell_+^2\right)(\mathrm{grad}\, u)(\gamma_i^k), \tag{23}$$

where $\ell_- := |\gamma_i^k - \gamma_{i-1}^k|$, $\ell_+ := |\gamma_{i+1}^k - \gamma_i^k|$ and

$$w_- := \frac{\ell_+ e^{u(\gamma_{i-1}^k)}}{\ell_+ e^{u(\gamma_{i-1}^k)} + \ell_- e^{u(\gamma_{i+1}^k)}}, \quad w_+ := \frac{\ell_- e^{u(\gamma_{i+1}^k)}}{\ell_+ e^{u(\gamma_{i-1}^k)} + \ell_- e^{u(\gamma_{i+1}^k)}}.$$

F.2.2 Controlling Topology. Although the topology of the resulting field $\mathbf{B}$ is initially fixed by the matching (cf. Sec. 7.2) of the red and blue points and the choice of geodesics for the connections (cf. Sec. 5.2), large update steps may lead to field lines crossing. To prevent this we bound the magnitude of updates by the tube radius. Moreover, we cut off field lines reaching beyond a threshold distance from the sun's surface. For the updates (23) of the resulting end points of the open field lines we use linear extrapolation.